



저작자표시-비영리-변경금지 2.0 대한민국

이용자는 아래의 조건을 따르는 경우에 한하여 자유롭게

- 이 저작물을 복제, 배포, 전송, 전시, 공연 및 방송할 수 있습니다.

다음과 같은 조건을 따라야 합니다:



저작자표시. 귀하는 원저작자를 표시하여야 합니다.



비영리. 귀하는 이 저작물을 영리 목적으로 이용할 수 없습니다.



변경금지. 귀하는 이 저작물을 개작, 변형 또는 가공할 수 없습니다.

- 귀하는, 이 저작물의 재이용이나 배포의 경우, 이 저작물에 적용된 이용허락조건을 명확하게 나타내어야 합니다.
- 저작권자로부터 별도의 허가를 받으면 이러한 조건들은 적용되지 않습니다.

저작권법에 따른 이용자의 권리는 위의 내용에 의하여 영향을 받지 않습니다.

이것은 [이용허락규약\(Legal Code\)](#)을 이해하기 쉽게 요약한 것입니다.

[Disclaimer](#)

교육학석사 학위논문

Geometrical Anatomy for the
Oxygen Vacancies in Epitaxial
 $\text{Hf}_{0.5}\text{Zr}_{0.5}\text{O}_2$ Film Grown by Atomic
Layer Deposition

원자층 증착법으로 성장한 단결정형 $\text{Hf}_{0.5}\text{Zr}_{0.5}\text{O}_2$
박막 내 산소 공공 생성에 대한 기하학적 분석

2024 년 8 월

서울대학교 대학원

과학교육과 물리전공

안 치 환

Geometrical Anatomy for the Oxygen Vacancies in Epitaxial $\text{Hf}_{0.5}\text{Zr}_{0.5}\text{O}_2$ Film Grown by Atomic Layer Deposition

원자층 증착법으로 성장한 단결정형 $\text{Hf}_{0.5}\text{Zr}_{0.5}\text{O}_2$
박막 내 산소 공공 생성에 대한 기하학적 분석

지도 교수 채 승 철

이 논문을 교육학석사 학위논문으로 제출함
2024 년 8 월

서울대학교 대학원
과학교육과 물리전공
안 치 환

안치환의 교육학석사 학위논문을 인준함
2024 년 8 월

위 원 장 _____ 조 정 효 (인)

부위원장 _____ 석 효 준 (인)

위 원 _____ 채 승 철 (인)

Abstract

We report on the selective influence of elastic strain on the formation of the oxygen deficiency in light of the optical response of epitaxial (001), (110), and (111)-oriented $\text{Hf}_{0.5}\text{Zr}_{0.5}\text{O}_2$ films grown by conventional yet unfamiliar atomic layer deposition for epitaxy. Optical spectroscopy was conducted using ultraviolet-visible spectroscopic ellipsometry for the $\text{Hf}_{0.5}\text{Zr}_{0.5}\text{O}_2$ films grown on yttria-stabilized zirconia substrates. The shallow trap level was dominantly observed in (111)-oriented $\text{Hf}_{0.5}\text{Zr}_{0.5}\text{O}_2$ film. X-ray photoemission spectroscopy demonstrated that the strong oxygen deficiency is preferred in the (111)-oriented $\text{Hf}_{0.5}\text{Zr}_{0.5}\text{O}_2$ film. Density functional theory calculations of oxygen vacancy formation energy also showed a pronounced preference for oxygen deficiency in the (111) orientation. This selective formation of oxygen vacancies in the (111)-oriented $\text{Hf}_{0.5}\text{Zr}_{0.5}\text{O}_2$ film suggests that the latent phenomena associated with oxygen defects in the functional $\text{Hf}_{0.5}\text{Zr}_{0.5}\text{O}_2$ film are partly attributed to the (111) directional strain.

Keyword : oxygen vacancy, defects, $\text{Hf}_{0.5}\text{Zr}_{0.5}\text{O}_2$, Epitaxial, thin film

Student Number : 2022-27471

Table of Contents

Abstract	i
Contents.....	ii
List of Table.....	iii
List of Figure	iii
I. Introduction.....	1
II. Material and methods	3
III. Results and discussion	5
3.1. Structural analysis of epitaxial $\text{Hf}_{0.5}\text{Zr}_{0.5}\text{O}_2$ thin film.....	5
3.2. Optical properties of epitaxial $\text{Hf}_{0.5}\text{Zr}_{0.5}\text{O}_2$ thin films.....	8
3.3. Oxygen vacancies formation preference investigation	16
IV. Conclusions.....	24
References.....	25
Appendix	34
국문초록	53

List of Table

Table 1. DFT-calculated oxygen vacancy formation energy (E_{vac}) for various HZO domains under different epitaxial strains, as shown by X-ray RSM analysis: O-[010], O-[001], O-[110], O-[101], O-[111], T-[110], and T-[111]. The table lists the E_{vac} for different oxygen sites: $\text{O}_{\text{O}(3)}$ and $\text{O}_{\text{O}(4)}$ in orthorhombic phase, and $\text{T}_{\text{O}(1)}$ and $\text{T}_{\text{O}(2)}$ in tetragonal phase.	22
--	----

List of figure

Fig. 1. Schematic diagrams of epitaxial HZO thin films grown on the (a) (001), (b) (110), and (c) (111) YSZ substrates, respectively. Blue, green, and red solid circles indicate Hf, Zr, O atoms, respectively. X-ray diffraction profiles of 20 nm, 18 nm, and 16 nm-thick epitaxial HZO thin films on (d) (001), (e) (110), and (f) (111) YSZ substrates, respectively. X-ray RSM of 20 nm, 18 nm, and 16 nm-thick epitaxial HZO thin films grown on (g) (001), (h) (110), and (i) (111) YSZ substrates, respectively.	7
--	---

Fig. 2. Dielectric function (ϵ_1 , ϵ_2) of epitaxial HZO thin film layers on (a) (001), (b) (110), and (c) (111) YSZ substrates, respectively. Optical anisotropy was observed in (110)-oriented epitaxial HZO thin film.	10
--	----

Fig. 3. (a) Tauc plot of $(ah\nu)^2$ versus photon energy ($h\nu$). By extrapolating the linear section of graph to intercept, direct band gap energies of 5.90 eV, 5.81 eV (5.95 eV in x -direction), 5.78 eV were obtained for (001), (110), and (111)-oriented epitaxial HZO films, respectively. (b) The first derivative of the imaginary part of dielectric functions of HZO thin films with a distinct shoulder peak near 5.4 eV in the (111)-oriented epitaxial HZO film, unlike those in other orientations. 13

Fig. 4. Plot of $\ln(\alpha)$ versus photon energy just below the direct band gap to determinate Urbach energy of epitaxial HZO thin films on (a) (001), (b) (110), and (c) (111) YSZ substrates, respectively. 15

Fig. 5. High-resolution XPS spectra for (a) Hf 4f, (b) Zr 3d, and (c) O 1s on the surface of epitaxial HZO thin films with three different growth orientations after pre-sputtering. The figures in each row correspond to orientations of epitaxial HZO thin films, from top to bottom, (001), (110), and (111), respectively. 18

Fig. 6. (a) conventional non-strained orthorhombic HZO unit cell with oxygen atoms classified and labeled as $O_{O(1)}$, $O_{O(2)}$, $O_{O(3)}$, and $O_{O(4)}$. (b) conventional non-strained tetragonal HZO unit cell with oxygen

atoms classified and labeled as $T_{O(1)}$ and $T_{O(2)}$. The ordering of Hf (navy blue spheres) and Zr (green spheres) is shown, with the configurations of oxygen atoms (red spheres) indicated. The right panels show the unit cells with oxygen vacancy (transparent red dashed circle)20

I. Introduction

Emerging capability associated with inevitable defects in oxide thin films has been attracting interest due to their functional versatility by actionable external stimuli. For example, the meta-material form of HfO_2 with the matured integrity of the conventional complementary metal oxide semiconductor (CMOS) process demonstrated new functional operations known as memristive behavior and ferroelectricity.¹⁻⁶ As a form for the oxygen vacancies mediated mobile ionic channel in the insulating matrix, HfO_2 has attracted considerable interest as a promising CMOS-compatible memristive material due to its simple structure, fast switching speed (<10 ns) and low power consumption (<10 pJ).⁷⁻¹⁰ In addition, precise control of oxygen vacancies for the stabilization of the meta-stable orthorhombic HfO_2 phase exhibited unprecedented ferroelectricity with substantial remanent polarization between $10\text{-}40\text{ }\mu\text{C}/\text{cm}^2$.^{2, 11-13} These properties of HfO_2 film offer potential for emerging applications in nonvolatile memory and neuromorphic devices.¹⁴⁻¹⁷

In this regard, the concrete understanding of the formation and manipulation of oxygen deficiencies associated with the strain engineering is crucial in the scientific as well as application point of view.¹⁸⁻²¹ While strain engineering has been a key ingredient for adjusting the functionalities of HfO_2 films,²²⁻²⁴ it has primarily been targeted to modulate the structural phases. The other important but easily overlooked role of strain in oxides is controlling formation energy of oxygen vacancies. In high- T_C superconducting cuprates, for instance, strain engineering was utilized to modulate the T_C by changing crystal structures and resultant electronic band structures.^{25, 26} However, later investigations uncovered the easier

formation of oxygen vacancies by strain can significantly modulates the critical temperature by changing the level of hole doping.²⁷ For HfO_2 , it is also essential to examine the role of epitaxial strain, not only in terms of structural distortion but also in the formation of oxygen vacancies. Despite the importance of oxygen vacancy on the various properties of HfO_2 , the correlation between oxygen vacancy and strain has not yet been thoroughly investigated.

In this Letter, we demonstrate that the defect states of epitaxial $\text{Hf}_{0.5}\text{Zr}_{0.5}\text{O}_2$ (HZO) film grown by the conventional CMOS compatible atomic layer deposition (ALD) are notably influenced by anisotropic epitaxial strain. The three epitaxial (001), (110), and (111)-oriented HZO thin films were grown along the (001), (110), and (111) yttria-stabilized Zirconia (YSZ) substrates. Using the X-ray reciprocal space mapping (RSM), variations in epitaxial strain direction and magnitude were identified in three fully strained HZO thin films. Through meticulous spectroscopic ellipsometry analysis in the UV-vis spectrum, we identified the selective formation of defect states in HZO films with respect to the strain circumstances. Complementary X-ray photoelectron spectroscopy (XPS) was conducted to determine the stoichiometric differences and chemical configuration variations in the different HZO thin films based on their growth direction, revealing correlations with the Urbach energy from their optical responses. Effects of growth orientation and anisotropic epitaxial strain to oxygen vacancy formation energy was estimated by using density functional theory (DFT) calculations.

II. Material and methods

HZO thin films were grown on YSZ substrates with three different surface normal orientations using the conventional ALD process. Single-crystalline YSZ (9.5 mol% yttria) substrate was used for the epitaxial growth of HZO film with crystallographic controlled orientations of (001), (110), and (111). The precursors for hafnium and zirconium were used from Tetrakis (ethylmethylamino) hafnium (TEMAH) and Tetrakis (ethylmethylamino) zirconium (TEMAZ), respectively, which were heated to a temperature of 90°C prior to utilization. HZO thin films were deposited on YSZ substrates at 280°C in an ozone environment to facilitate oxidation during the ALD process. Structural characterization of the epitaxially grown HZO films on YSZ substrates was performed using a high-resolution X-ray diffractometer (XRD) (Discover D8, Bruker). The spectroscopic ellipsometry measurements of epitaxial HZO thin films were conducted over a spectral range of 0.74-6.47 eV at a fixed incident angle of 70° (M-2000, J. A. Woollam). The ellipsometry parameters were analyzed using a two-layer model, considering the atomically flat surface assessed by atomic force microscopy and the thickness of the thin film estimated by X-ray reflectivity (Appendix section 1). XPS analysis was conducted using a focused monochromatic Al K α X-ray source for excitation and a spherical section analyzer for detection (Versaprobe III system, ULvac-phi). The energy scales of the XPS spectra for the examined HZO thin films were calibrated using the binding energy of the C 1s peak at 284.4 eV. The calculations based on the DFT were performed with the projector-augmented wave (PAW) method as implemented in Vienna Ab initio Simulation Package (VASP) code.²⁸

Detailed methods of theoretical calculations are documented in the Appendix section 2.

III. Results and discussion

3.1. Structural analysis of epitaxial $\text{Hf}_{0.5}\text{Zr}_{0.5}\text{O}_2$ thin film

High-quality epitaxy is achieved in the HZO films grown by the conventional ALD method. Figure 1a-c show schematic representations of the epitaxial relationship of HZO thin films depending on the (001), (110), and (111) YSZ surfaces, respectively. With respect to the lattice coherence between orthorhombic (O)/tetragonal (T)-HZO and (001), (110), and (111) cubic YSZ surfaces, HZO thin films can be accommodated with three distinct different growth orientations. Considering the lattice constant of YSZ substrate (0.512 nm), the plausible orientations of HZO films were sketched in terms of the minimization of elastic tension. Figure 1d-f show the XRD θ - 2θ scans of the HZO thin films grown on (001), (110), and (111) YSZ substrates at identical growth condition, respectively. The diffraction patterns observed in the XRD θ - 2θ scans distinctly show single phase reflections at angles of 35° - 36° , 52° - 53° , and 30° - 31° , corresponding to the (002), (220), and (111) O/T-HZO reflections, respectively.²⁹ No significant peak shifts or secondary phases such as monoclinic phase were observed in the XRD θ - 2θ analysis of HZO thin films on (001), (110), and (111) YSZ substrates as shown in Figure A3 in Appendix section 1. Considering the epitaxial atomic stacking as illustrated schematically in Figure 1a-c, these XRD profiles are attributed to the (002), (220), and (111) reflection spectra of (001), (110), and (111)-oriented epitaxial HZO thin films coherently grown on the YSZ substrates, respectively.

The HZO thin film demonstrated an epitaxial in-plane coherence with the YSZ substrate. Figure 1g displays the X-ray RSM results near the YSZ (204) plane for ~20 nm-thick HZO thin film deposited on (001) YSZ substrate. The in-plane alignment of the peaks for both the HZO film and YSZ substrate at $Q_x \approx 0.39$ indicates that the in-plane crystallinity of the HZO films is highly coherent with the YSZ substrate. The X-ray RSM results displayed in Figure 1h and 1i similarly demonstrate the alignment results for HZO thin films grown on (110) and (111) YSZ substrates, respectively. Considering the lattice parameters of the HZO polymorphs presented in Table A2 with a Poisson's ratio of 0.3,^{30, 31} and the methodology and results for identically synthesized samples in our previous study,³² we calculated the volumetric strain values and determined the plausible crystallographic domains in the epitaxial HZO thin films. As an example, on the (001) YSZ substrate, we identified two types of HZO domains: [001] out-of-plane directed orthorhombic (O-[001]), and [010] out-of-plane directed orthorhombic (O-[010]) HZO, each exhibiting distinct strain characteristics. For detailed analysis of exact strain values and other plausible domains, see the Table A3 in Appendix section 3. These crystal alignments enabled us to investigate the epitaxial strain effect on the optical properties and defect formation in the fully strained HZO thin films.

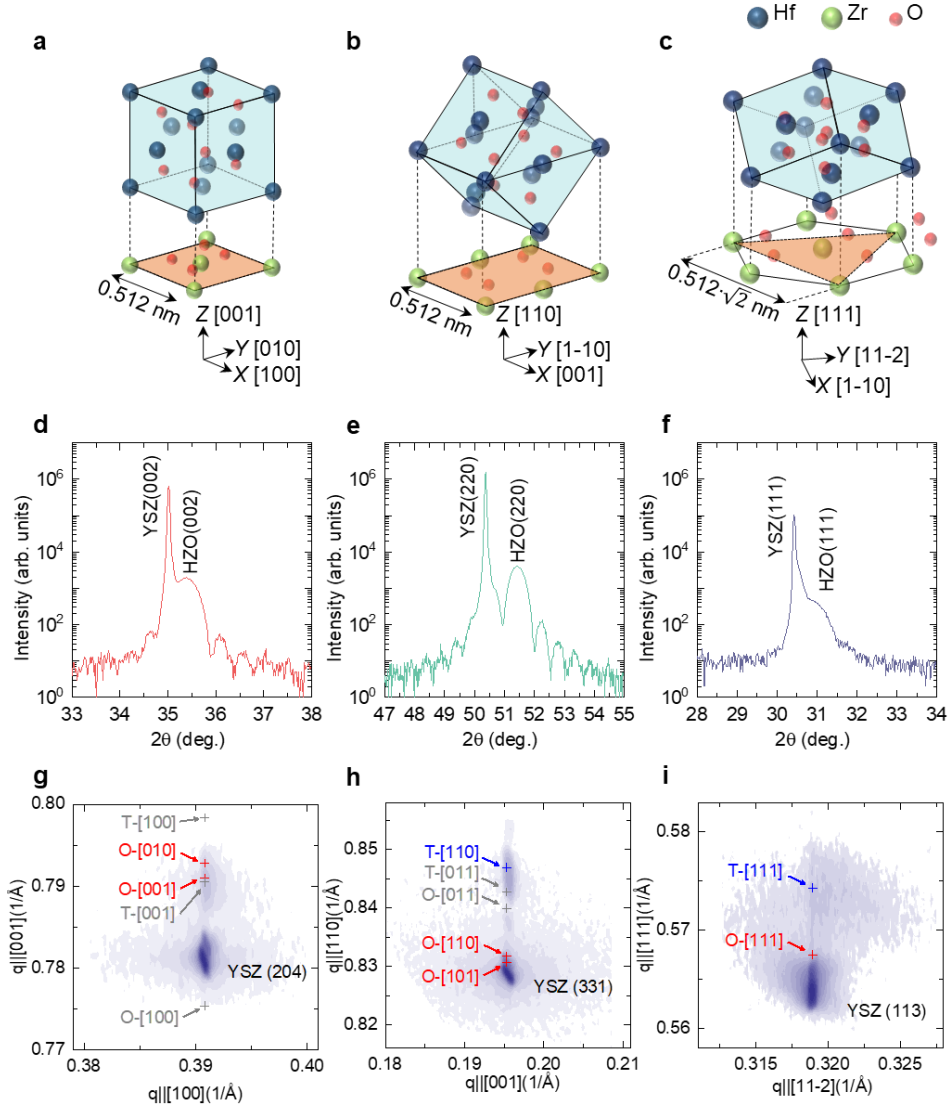


Fig. 1. Schematic diagrams of epitaxial HZO thin films grown on the (a) (001), (b) (110), and (c) (111) YSZ substrates, respectively. Blue, green, and red solid circles indicate Hf, Zr, O atoms, respectively. X-ray diffraction profiles of 20 nm, 18 nm, and 16 nm-thick epitaxial HZO thin films on (d) (001), (e) (110), and (f) (111) YSZ substrates, respectively. X-ray RSM of 20 nm, 18 nm, and 16 nm-thick epitaxial HZO thin films grown on (g) (001), (h) (110), and (i) (111) YSZ substrates, respectively.

3.2. Optical properties of epitaxial $\text{Hf}_{0.5}\text{Zr}_{0.5}\text{O}_2$ thin films

Systematic variations of dielectric constants in UV-vis optical spectroscopy were observed depending on the crystallographic orientation of epitaxial HZO thin films. Figure 2a-c display the complex dielectric function, ϵ_1 and ϵ_2 (real and imaginary components), for the (001), (110), and (111)-oriented epitaxial HZO thin films. All optical spectra of HZO films grown on (001), (110), and (111) YSZ substrates showed transparency up to nearly 5 eV, followed by the onset of absorption,³³⁻³⁵ The conventional dielectric response of a wide band gap semiconductor, indicated by a sudden increase in the imaginary component in the UV region, corresponds to absorption due to inter-band transition between the highest occupied valence band states and the lowest conduction band states. In our case, this transition is known to occur from non-bonding O 2p states forming the top of the valence band to anti-bonding Hf/Zr 5d/4d states, which are the primary contributors to the conduction band.^{36, 37}

Optical anisotropy was observed in the (110)-oriented HZO thin film, characterized by anisotropic directional dielectric function components (ϵ_x and ϵ_y , where x and y are the directions depicted in Figure 1b), as shown in Figure 2b. Orthorhombic, and tetragonal phase intrinsically has biaxial and uniaxial optical anisotropy, respectively, due to its structural asymmetry, as shown in Figure A4 in Appendix section 4. DFT-calculated dielectric function of each HZO domains in (001), (110), and (111)-oriented films also shows biaxial optical anisotropy, as shown in Figure A5. The experimental absence of optical anisotropy in (001) and (111)-oriented HZO films might be attributed to in-plane mixing of rotational

domains. 90° and 120° azimuthal rotations of HZO domains grown on (001) and (111) YSZ substrates, respectively, only change the direction of strain, not its magnitude. This rotation-independent strain magnitude is originated from square and equilateral triangle surface of (001) and (111) YSZ surface, respectively. As a result, the in-plane directions of the HZO domains grown on (001) and (111) YSZ are unlikely to be uniquely determined by those of substrate. In contrast, when HZO domains on (110) YSZ substrates is azimuthally rotated, the domains experience significant changes in in-plane strain, due to rectangular surface of (110) YSZ. In our prior report for identically grown sample, the presence of only two well-defined diffraction peak patterns in X-ray ϕ -scan patterns demonstrates absence of in-plane rotated domains in (110)-oriented HZO film.³² Consequently, the in-plane directions are likely to be uniquely determined by those of substrate. These difference relations in interface of film and substrate could lead to dominantly observed optical anisotropy in (110)-oriented d HZO thin film.

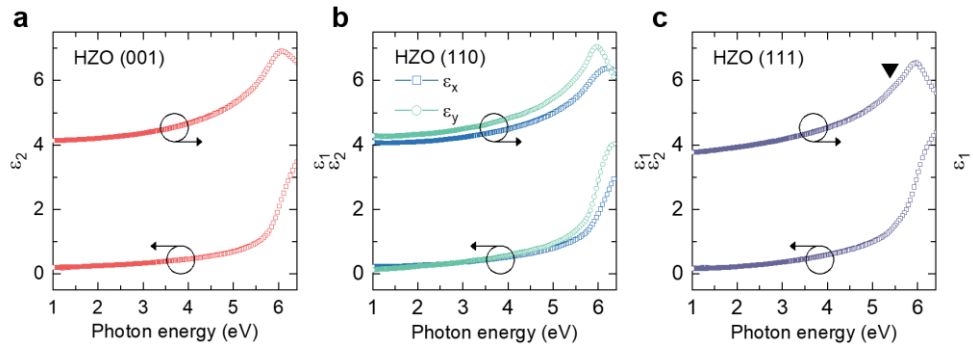


Fig. 2. Dielectric function (ϵ_1 , ϵ_2) of epitaxial HZO thin film layers on (a) (001), (b) (110), and (c) (111) YSZ substrates, respectively. Optical anisotropy was observed in (110)-oriented epitaxial HZO thin film.

The strain mediated direct band gap variation was observed in the distinct (001), (110), and (111)-oriented HZO films. The systematic shift in the onset of direct transition was estimated using Tauc plots of $(\alpha h\nu)^2$ for the direct band gap, as shown in Figure 3a. In the Tauc plot, the absorption coefficient α was formulated as $\alpha = 4\pi k/\lambda$, where k and λ represent the extinction coefficient and the wavelength of the incident light, respectively. The direct band gaps of the (001), (110), and (111)-oriented epitaxial HZO films were found to be 5.90 eV, 5.81 eV (5.95 eV), and 5.78 eV, respectively, by extrapolating the linear portions of the Tauc plots to intersect at the zero point. Note that the value in the parenthesis is for the case of absorption through x -direction (as depicted in Figure 1b) in the (110)-oriented epitaxial HZO thin film whereas the value of 5.81 eV is from the absorption through y -direction. As shown in Figure A6, orthorhombic HZO exhibits a lower conduction band minimum and total density of states compared to tetragonal HZO. As a result, the variation of the direct band gap might be occurred in the orthorhombic domains. Additionally, considering the structural differences of HZO thin films grown on surface different YSZ substrates, this variation of direct band gap can be attributed to differences in epitaxial strain and the domain distributions associated with the distinct surface orientation of the YSZ substrate.³⁸⁻⁴¹

The shoulder peak observed in dielectric function of the (111)-oriented epitaxial HZO thin films is associated with oxygen vacancies. Figure 3b presents the first derivative graph of the ϵ_2 of HZO thin films, highlighting the shoulder peak in the (111)-oriented epitaxial HZO thin film within the photon energy range of 5.0 to 5.75 eV. The shoulder peak near 5.4 eV in the (111)-oriented epitaxial HZO thin film suggests the potential existence of shallow trap level, contrasting

with the smooth band edges in other (001) and (110) orientations. Previous research on HfO_2 thin films has often linked such a shoulder peak to the monoclinic phase or polycrystalline HfO_2 films, implying intrinsic crystal structure as its source.^{42, 43} However, taking into account the large-range X-ray diffraction in Figure A3 without strong evidences of the monoclinic or polycrystal phase, it is plausible to consider other origins for shallow trap levels approximately 0.3-0.4 eV below the conduction band or above the valence band. Oxygen vacancies could be the cause of the defect-induced shoulder peak, as the defect states of oxygen vacancies or interstitial oxygen are found near the band edges of HfO_2 .⁴⁴⁻⁴⁷

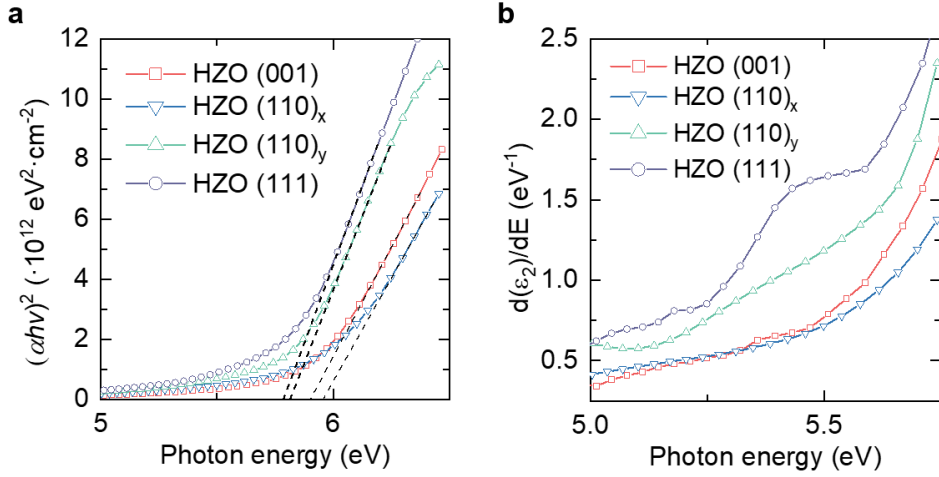


Fig. 3. (a) Tauc plot of $(\alpha h\nu)^2$ versus photon energy ($h\nu$). By extrapolating the linear section of graph to intercept, direct band gap energies of 5.90 eV, 5.81 eV (5.95 eV in x -direction), 5.78 eV were obtained for (001), (110), and (111)-oriented epitaxial HZO films, respectively. (b) The first derivative of the imaginary part of dielectric functions of HZO thin films with a distinct shoulder peak near 5.4 eV in the (111)-oriented epitaxial HZO film, unlike those in other orientations.

Variations in defect states associated with the orientation of epitaxial HZO thin film were quantified by observing changes of Urbach energy (E_U). Defect states lead to the formation of an absorption tail extending into the forbidden gap, known as the Urbach tail. To describe this tail, we used the Urbach equation formulated as $\alpha(E) = \alpha_0 \exp(E / E_U)$,⁴⁸ with E_U quantifying the energetic sharpness of the band edge, where α , E , α_0 , are the absorption coefficient, photon energy and material constant, respectively. Figure 4a-c show the Urbach energy curves of (001), (110), and (111)-oriented epitaxial HZO thin film, respectively. To calculate Urbach energy, the natural logarithm of the absorption coefficient ($\ln\alpha$) is plotted against the photon energy ($h\nu$) and the Urbach energy value is obtained from the reciprocal of the slope in the linear region just below the direct band gap. The Urbach energy values in (001), (110), and (111)-oriented epitaxial HZO thin films are estimated to 0.61 eV, 0.76 eV (0.86 eV), and 0.86 eV, respectively. Note that the (110)-oriented epitaxial HZO thin film has two different values, 0.76 eV in x -direction, and 0.86 eV in y -direction, respectively, due to its optical anisotropy, i.e., direction is depicted in Figure 1b. The increase in Urbach energy indicates that variations in defects states arising from structural disorder or oxygen vacancies are highly correlated with the preferred growth orientation and the associated epitaxial strain.^{35, 49-52}

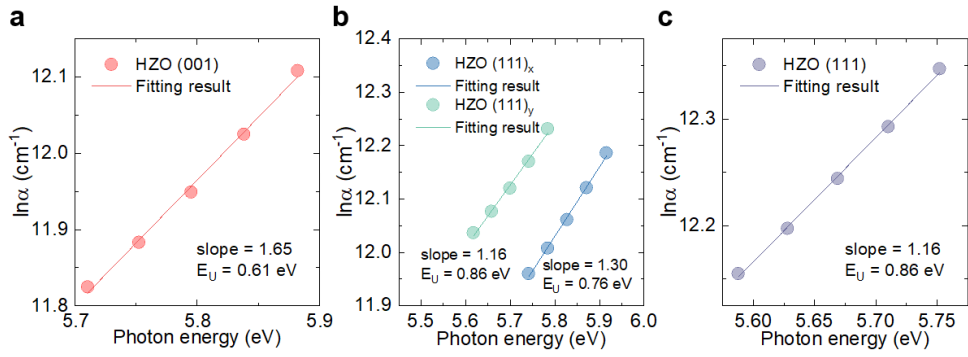


Fig. 4. Plot of $\ln(\alpha)$ versus photon energy just below the direct band gap to determinate Urbach energy of epitaxial HZO thin films on (a) (001), (b) (110), and (c) (111) YSZ substrates, respectively.

3.3. Oxygen vacancies formation preference investigation

Oxygen vacancies are responsible to the defect states with respect to the orientation of epitaxial HZO thin films. To further examine the oxidation states of Hf and Zr on the film surface, XPS was utilized for the characterization of the epitaxial HZO thin films. Figure 5a-c show the narrow-scan XPS spectra of Hf 4f, Zr 3d, and O 1s peaks on the surfaces of epitaxial HZO thin films grown on various YSZ substrates, respectively, after pre-sputtering. The O 1s XPS deconvolution reveals two peaks at 529.9 eV and 531.3 eV (Figure 2c). The first peak corresponds to lattice oxygen in HfO_2 and ZrO_2 , while the second peak is due to weakly bound adsorbed oxygen on the sample surface. The maximums of Hf 4f_{7/2} and Zr 3d_{5/2} at the energy of 16.5 eV and 181.9 eV correspond to the Hf^{4+} and Zr^{4+} states, respectively, and coincide with the energy positions observed in stoichiometric HfO_2 and ZrO_2 .⁵³ The deconvolution of Hf 4f and Zr 3d lines into separate components revealed additional peaks at energy values of 15.7 eV and 180.9 eV as shown in Figure 5a and 5b with filled blue and green color spectra, respectively. These peaks suggest the presence of nonstoichiometric oxides (HfO_{2-x} and ZrO_{2-x}), indicating the generation of oxygen vacancies within the films.^{54, 55} The concentrations of Hf and Zr with lower oxidation states were estimated to be 1.95%, 2.87%, and 4.80% for Hf and 1.98%, 4.10%, and 11.35% for Zr in the (001), (110), and (111) orientations, respectively. This increase of the concentrations, associated with the amount of oxygen vacancies in (100), (110), and (111)-oriented epitaxial HZO thin films, correlates with the increase in Urbach energy aforementioned. Therefore, it can be argued that the differences in defect states according to the

growth direction of epitaxial HZO thin films are primarily caused by oxygen vacancies.

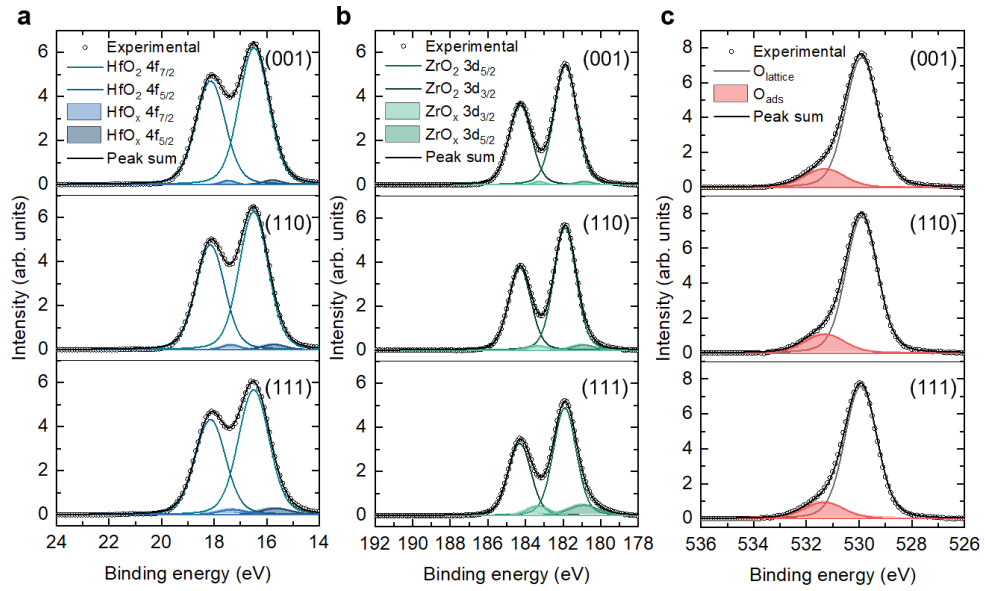


Fig. 5. High-resolution XPS spectra for (a) Hf 4f, (b) Zr 3d, and (c) O 1s on the surface of epitaxial HZO thin films with three different growth orientations after pre-sputtering. The figures in each row correspond to orientations of epitaxial HZO thin films, from top to bottom, (001), (110), and (111), respectively.

Density functional theory calculations were employed to investigate oxygen vacancy formation energy (E_{vac}) along various growth orientations. To investigate computationally disparities in the possibility of oxygen vacancy formation across three growth orientations, we conducted first principles calculations based on DFT. The two types of pristine supercells were created based on the conventional unit cells with/without strain estimated from the experimental X-ray RSM results in Figure 1g-i. The defective supercells were created by removing single oxygen atom from each pristine supercell. The oxygen vacancy formation energy was calculated as the total energy difference between the defective and pristine supercells, adjusted for the chemical potential of oxygen : $E(\text{defective}) - E(\text{pristine}) + \mu(\text{O}_2)/2$ where $E(\text{defective})$ and $E(\text{pristine})$ represent the total energy of the supercells with and without an oxygen vacancy, respectively, and $\mu(\text{O}_2)$ is the total energy of an O_2 molecule. Figure 6a and 6b show schematic diagrams of conventional orthorhombic and tetragonal unit cells with the oxygen atoms of different symmetric coordinate numbers. The configuration of the oxygen sites was determined by considering the bond lengths and angles of Hf-O and Zr-O. Each oxygen atom with different coordinate numbers labeled as $\text{O}_{\text{O}(n)}$ and $\text{T}_{\text{O}(n)}$ was removed in orthorhombic and tetragonal phases, respectively, and total energy was estimated. The oxygen vacancy is placed in the schematic diagrams with transparent red dashed circles in right panels of Figure 6a and 6b.

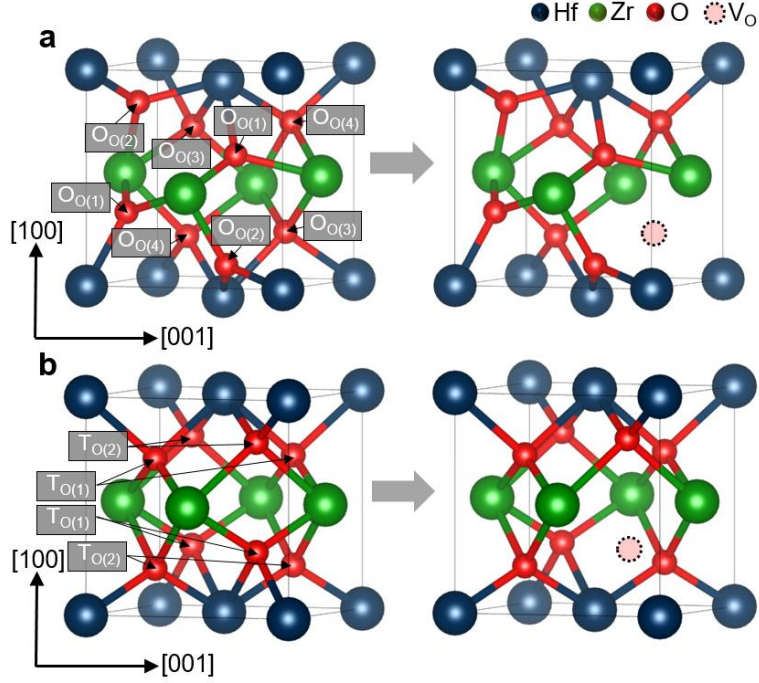


Fig. 6. (a) conventional non-strained orthorhombic HZO unit cell with oxygen atoms classified and labeled as O_O(1), O_O(2), O_O(3), and O_O(4). (b) conventional non-strained tetragonal HZO unit cell with oxygen atoms classified and labeled as T_O(1) and T_O(2). The ordering of Hf (navy blue spheres) and Zr (green spheres) is shown, with the configurations of oxygen atoms (red spheres) indicated. The right panels show the unit cells with oxygen vacancy (transparent red dashed circle)

The preference for oxygen vacancies formation in (111)-oriented epitaxial HZO thin films can be attributed to the strain-induced thermodynamical lowering of formation energy. First, for the supercells without strain, E_{vac} for all the distinct oxygen sites were calculated and listed in Table A3. For the non-strained orthorhombic phase, the E_{vac} for the tri-coordinated $\text{O}_{\text{O}(1)}$ and $\text{O}_{\text{O}(2)}$ sites, i.e., oxygens bonded with three neighbor metal atoms, is 0.1-0.3 eV higher than for the tetra-coordinated $\text{O}_{\text{O}(3)}$ and $\text{O}_{\text{O}(4)}$ sites, i.e., oxygens bonded with four neighbor metal atoms, consistent with earlier report for HfO_2 .⁵⁶ Based on the overall higher E_{vac} for tri-coordinated oxygen sites, the E_{vac} calculations for strained orthorhombic supercells were conducted only with tetra-coordinated oxygen sites.⁵⁶ As shown in Table 1, the strained orthorhombic phases exhibit a pronounced decrease in E_{vac} , ranging from 7.9 to 7.4 eV, in the sequence of supercell reflecting (001), (110), and (111)-oriented epitaxial HZO thin films, with E_{vac} for $\text{O}_{\text{O}(3)}$ being lower than that for $\text{O}_{\text{O}(4)}$. This result resembles the tendencies observed in Urbach energy and XPS analysis, suggesting that the defect states observed in the optical response are closely related to oxygen vacancies. However, in the strained tetragonal phase, the difference in E_{vac} between supercells reflecting (110) and (111)-oriented HZO thin films is an order of magnitude smaller than in the strained orthorhombic phase. The similarity of formation energy between strained (110) and (111) tetragonal phases might not be responsible for the difference of defect states observed in the optical response and sub-oxide Hf/Zr concentrations estimated by XPS analysis. In addition, considering the absence of tetragonal phase in the (001)-oriented HZO film, the formation of oxygen vacancies in the tetragonal phase is far from this discussion. Consequently, the tendency for oxygen vacancy formation along the

growth direction is due to the formation of oxygen vacancies in the orthorhombic HZO phase with the less vacancy contribution of tetragonal phase.

Table 1. DFT-calculated oxygen vacancy formation energy (E_{vac}) for various HZO domains under different epitaxial strains, as shown by X-ray RSM analysis: O-[010], O-[001], O-[110], O-[101], O-[111], T-[110], and T-[111]. The table lists the E_{vac} for different oxygen sites: $O_{O(3)}$ and $O_{O(4)}$ in orthorhombic phase, and $T_{O(1)}$ and $T_{O(2)}$ in tetragonal phase.

YSZ surface	Domain	E_{vac} (eV) for oxygen sites			
		$O_{O(3)}$	$O_{O(4)}$	$T_{O(1)}$	$T_{O(2)}$
(001)	O-[010]	7.81	7.87	—	—
	O-[001]	7.80	7.86	—	—
(110)	O-[110]	7.53	7.60	—	—
	O-[101]	7.57	7.64	—	—
	T-[110]	—	—	7.51	7.28
(111)	O-[111]	7.40	7.48	—	—
	T-[111]	—	—	7.51	7.28

Selective strain control of HZO via the crystallographic direction of substrate suggests a geometric preference for forming defects, especially oxygen vacancies, in epitaxial HZO thin films. Our comprehensive study of epitaxial HZO thin films, grown on (001), (110), and (111) YSZ substrates using ALD, has provided significant insights into how substrate orientation influences film properties. X-ray RSM profiles reveal that the surface orientation of the YSZ substrate influences the film growth direction and epitaxy, enabling possible variations in defect states and phase formation according to growth direction. The distinctive shoulder peak of UV-vis spectroscopy observed in the (111)-oriented epitaxial HZO thin film, along with variations in the Urbach energy, indicates a strong correlation between oxygen vacancies and defect states in these films. This correlation is further supported by quantitative analysis of sub-oxide Hf/Zr and oxygen vacancies through XPS, and by DFT calculations of oxygen vacancy formation energy, revealing a clear orientation-dependent trend. The systematic changes according to the direction and magnitude of epitaxial strain suggest the potential to control oxygen vacancy formation through the epitaxial strain and surface orientation of the substrate.

IV. Conclusions

In summary, we have investigated the selective influence of epitaxial strain on the formation and manipulation of oxygen vacancies in the epitaxial HZO films grown by ALD. Through comprehensive XRD and X-ray RSM analyses, we have elucidated the crystallographic orientation and strain in the thin film structure. Spectroscopic ellipsometry measurements revealed significant anisotropy, shifts in the direct band gap and the variations and emergence of defect levels, particularly in (111)-oriented epitaxial HZO film. Further chemical characterization through XPS provided understanding of the stoichiometric variations across different film orientations. Additionally, DFT calculations show how epitaxial strain, according with the surface orientation of substrate, affects oxygen vacancy formation, consistent with experimental results. This insight paves the way for novel approaches in tailoring defect configuration and material functionality for broad technological applications.

References

- (1) Salahuddin, S.; Ni, K.; Datta, S. The era of hyper-scaling in electronics. *Nat. Electron.* 2018, 1 (8), 442-450.
- (2) Park, M. H.; Lee, Y. H.; Kim, H. J.; Kim, Y. J.; Moon, T.; Kim, K. D.; Mueller, J.; Kersch, A.; Schroeder, U.; Mikolajick, T. Ferroelectricity and antiferroelectricity of doped thin HfO₂-based films. *Adv. Mater.* 2015, 27 (11), 1811-1831.
- (3) Böске, T.; Müller, J.; Bräuhäus, D.; Schröder, U.; Böttger, U. Ferroelectricity in hafnium oxide thin films. *Appl. Phys. Lett.* 2011, 99 (10), 102903.
- (4) Lee, H.-J.; Lee, M.; Lee, K.; Jo, J.; Yang, H.; Kim, Y.; Chae, S. C.; Waghmare, U.; Lee, J. H. Scale-free ferroelectricity induced by flat phonon bands in HfO₂. *Science* 2020, 369 (6509), 1343-1347.
- (5) Yun, Y.; Buragohain, P.; Li, M.; Ahmadi, Z.; Zhang, Y.; Li, X.; Wang, H.; Li, J.; Lu, P.; Tao, L. Intrinsic ferroelectricity in Y-doped HfO₂ thin films. *Nat. Mater.* 2022, 21 (8), 903-909.
- (6) Banerjee, W.; Kashir, A.; Kamba, S. Hafnium oxide (HfO₂)—a multifunctional oxide: a review on the prospect and challenges of hafnium oxide in resistive switching and ferroelectric memories. *Small* 2022, 18 (23), 2107575.

- (7) Zhang, Y.; Mao, G.-Q.; Zhao, X.; Li, Y.; Zhang, M.; Wu, Z.; Wu, W.; Sun, H.; Guo, Y.; Wang, L. Evolution of the conductive filament system in HfO₂-based memristors observed by direct atomic-scale imaging. *Nat. Commun.* 2021, 12 (1), 7232.
- (8) Wu, Q.; Banerjee, W.; Cao, J.; Ji, Z.; Li, L.; Liu, M. Improvement of durability and switching speed by incorporating nanocrystals in the HfO_x based resistive random access memory devices. *Appl. Phys. Lett.* 2018, 113 (2), 023105.
- (9) Peng, Z.; Wu, F.; Jiang, L.; Cao, G.; Jiang, B.; Cheng, G.; Ke, S.; Chang, K. C.; Li, L.; Ye, C. HfO₂-based memristor as an artificial synapse for neuromorphic computing with tri-layer HfO₂/BiFeO₃/HfO₂ design. *Adv. Funct. Mater.* 2021, 31 (48), 2107131.
- (10) Lin, K.-L.; Hou, T.-H.; Shieh, J.; Lin, J.-H.; Chou, C.-T.; Lee, Y.-J. Electrode dependence of filament formation in HfO₂ resistive-switching memory. *J. Appl. Phys.* 2011, 109 (8), 084104.
- (11) Hoffmann, M.; Schroeder, U.; Schenk, T.; Shimizu, T.; Funakubo, H.; Sakata, O.; Pohl, D.; Drescher, M.; Adelman, C.; Materlik, R. Stabilizing the ferroelectric phase in doped hafnium oxide. *J. Appl. Phys.* 2015, 118 (7), 072006.
- (12) Pešić, M.; Fengler, F. P. G.; Larcher, L.; Padovani, A.; Schenk, T.; Grimley, E. D.; Sang, X.; LeBeau, J. M.; Slesazeck, S.; Schroeder, U.

Physical mechanisms behind the field-cycling behavior of HfO₂-based ferroelectric capacitors. *Adv. Funct. Mater.* 2016, 26 (25), 4601-4612.

(13) Starschich, S.; Menzel, S.; Böttger, U. Evidence for oxygen vacancies movement during wake-up in ferroelectric hafnium oxide. *Appl. Phys. Lett.* 2016, 108 (3), 032903.

(14) Wang, Y.; Liu, Q.; Long, S.; Wang, W.; Wang, Q.; Zhang, M.; Zhang, S.; Li, Y.; Zuo, Q.; Yang, J. Investigation of resistive switching in Cu-doped HfO₂ thin film for multilevel non-volatile memory applications. *Nanotechnology* 2009, 21 (4), 045202.

(15) Max, B.; Hoffmann, M.; Mulaosmanovic, H.; Slesazeck, S.; Mikolajick, T. Hafnia-based double-layer ferroelectric tunnel junctions as artificial synapses for neuromorphic computing. *ACS Appl. Electron. Mater.* 2020, 2 (12), 4023-4033.

(16) Kim, M.-K.; Lee, J.-S. Ferroelectric analog synaptic transistors. *Nano Lett.* 2019, 19 (3), 2044-2050.

(17) Chen, L.; Wang, T.-Y.; Dai, Y.-W.; Cha, M.-Y.; Zhu, H.; Sun, Q.-Q.; Ding, S.-J.; Zhou, P.; Chua, L.; Zhang, D. W. Ultra-low power Hf_{0.5}Zr_{0.5}O₂ based ferroelectric tunnel junction synapses for hardware neural network applications. *Nanoscale* 2018, 10 (33), 15826-15833.

- (18) Schlom, D. G.; Chen, L.-Q.; Fennie, C. J.; Gopalan, V.; Muller, D. A.; Pan, X.; Ramesh, R.; Uecker, R. Elastic strain engineering of ferroic oxides. *MRS Bull.* 2014, 39 (2), 118-130.
- (19) Ruf, J. P.; Paik, H.; Schreiber, N. J.; Nair, H. P.; Miao, L.; Kawasaki, J. K.; Nelson, J. N.; Faeth, B. D.; Lee, Y.; Goodge, B. H. Strain-stabilized superconductivity. *Nat. Commun.* 2021, 12 (1), 59.
- (20) Sando, D.; Agbelele, A.; Rahmedov, D.; Liu, J.; Rovillain, P.; Toulouse, C.; Infante, I.; Pyatakov, A.; Fusil, S.; Jacquet, E. Crafting the magnonic and spintronic response of BiFeO₃ films by epitaxial strain. *Nat. Mater.* 2013, 12 (7), 641-646.
- (21) Yang, M.; Yang, Y.; Hong, B.; Wang, L.; Hu, K.; Dong, Y.; Xu, H.; Huang, H.; Zhao, J.; Chen, H. Suppression of structural phase transition in VO₂ by epitaxial strain in vicinity of metal-insulator transition. *Sci. Rep.* 2016, 6 (1), 23119.
- (22) Liu, S.; Hanrahan, B. M. Effects of growth orientations and epitaxial strains on phase stability of HfO₂ thin films. *Phys. Rev. Mater.* 2019, 3 (5), 054404.
- (23) Qi, Y.; Singh, S.; Lau, C.; Huang, F.-T.; Xu, X.; Walker, F. J.; Ahn, C. H.; Cheong, S.-W.; Rabe, K. M. Stabilization of competing ferroelectric phases of HfO₂ under epitaxial strain. *Phys. Rev. Lett.* 2020, 125 (25), 257603.

- (24) Estandia, S.; Dix, N.; Gazquez, J.; Fina, I.; Lyu, J.; Chisholm, M. F.; Fontcuberta, J.; Sanchez, F. Engineering ferroelectric $\text{Hf}_{0.5}\text{Zr}_{0.5}\text{O}_2$ thin films by epitaxial stress. *ACS Appl. Electron. Mater.* 2019, 1 (8), 1449-1457.
- (25) Ivashko, O.; Horio, M.; Wan, W.; Christensen, N.; McNally, D.; Paris, E.; Tseng, Y.; Shaik, N.; Rønnow, H.; Wei, H. Strain-engineering mott-insulating La_2CuO_4 . *Nat. Commun.* 2019, 10 (1), 786.
- (26) Choi, E.-M.; Di Bernardo, A.; Zhu, B.; Lu, P.; Alpern, H.; Zhang, K. H.; Shapira, T.; Feighan, J.; Sun, X.; Robinson, J. 3D strain-induced superconductivity in $\text{La}_2\text{CuO}_{4+\delta}$ using a simple vertically aligned nanocomposite approach. *Sci. Adv.* 2019, 5 (4), eaav5532.
- (27) Meyer, T. L.; Jacobs, R.; Lee, D.; Jiang, L.; Freeland, J. W.; Sohn, C.; Egami, T.; Morgan, D.; Lee, H. N. Strain control of oxygen kinetics in the Ruddlesden-Popper oxide $\text{La}_{1.85}\text{Sr}_{0.15}\text{CuO}_4$. *Nat. Commun.* 2018, 9 (1), 92.
- (28) Kresse, G.; Joubert, D. From ultrasoft pseudopotentials to the projector augmented-wave method. *Phys. Rev. B* 1999, 59 (3), 1758.
- (29) Zhang, Z.; Hsu, S.-L.; Stoica, V. A.; Paik, H.; Parsonnet, E.; Qualls, A.; Wang, J.; Xie, L.; Kumari, M.; Das, S.; et al. Epitaxial Ferroelectric $\text{Hf}_{0.5}\text{Zr}_{0.5}\text{O}_2$ with Metallic Pyrochlore Oxide Electrodes. *Adv. Mater.* 2021, 33 (10), 1521-4095.
- (30) De Jong, M.; Chen, W.; Angsten, T.; Jain, A.; Notestine, R.; Gamst, A.; Sluiter, M.; Krishna Ande, C.; Van Der Zwaag, S.; Plata, J. J. Charting the

complete elastic properties of inorganic crystalline compounds. *Sci. Data* 2015, 2 (1), 1-13.

(31) Materlik, R.; Künneth, C.; Kersch, A. The origin of ferroelectricity in $\text{Hf}_{1-x}\text{Zr}_x\text{O}_2$: A computational investigation and a surface energy model. *J. Appl. Phys.* 2015, 117 (13), 134109.

(32) Cho, J. W.; Song, M. S.; Choi, I. H.; Go, K. J.; Han, J.; Lee, T. Y.; An, C.; Choi, H. J.; Sohn, C.; Park, M. H. Atomic Layer Deposition of Epitaxial Ferroelectric $\text{Hf}_{0.5}\text{Zr}_{0.5}\text{O}_2$ Thin Films. *Adv. Funct. Mater.* 2024, 34 (24), 2314396.

(33) Franta, D.; Ohlídal, I.; Nečas, D.; Vižd'a, F.; Caha, O.; Hasoň, M.; Pokorný, P. Optical characterization of HfO_2 thin films. *Thin Solid Films* 2011, 519 (18), 6085-6091.

(34) Khoshman, J. M.; Kordesch, M. E. Optical properties of a- HfO_2 thin films. *Surf. Coat. Technol.* 2006, 201 (6), 3530-3535.

(35) Martínez, F.; Toledano-Luque, M.; Gandía, J.; Cárabe, J.; Bohne, W.; Röhrich, J.; Strub, E.; Mártel, I. Optical properties and structure of HfO_2 thin films grown by high pressure reactive sputtering. *J. Phys. D: Appl. Phys.* 2007, 40 (17), 5256.

(36) Yang, X.; Zhou, T.; Hua, E.; Wang, Z.; Liu, Z.; Wang, H.; Liu, Q. Composition-dependent structure and bandgaps in $\text{Hf}_x\text{Zr}_{1-x}\text{O}_2$ thin films. *Appl. Phys. Lett.* 2024, 124 (12), 122902.

- (37) Fan, X.; Liu, H.; Zhong, B.; Fei, C.; Wang, X.; Wang, Q. Optical characteristics of H₂O-based and O₃-based HfO₂ films deposited by ALD using spectroscopy ellipsometry. *Appl. Phys. A: Mater. Sci. Process.* 2015, 119, 957-963.
- (38) Vailionis, A.; Boschker, H.; Siemons, W.; Houwman, E. P.; Blank, D. H.; Rijnders, G.; Koster, G. Misfit strain accommodation in epitaxial ABO₃ perovskites: Lattice rotations and lattice modulations. *Phys. Rev. B* 2011, 83 (6), 064101.
- (39) Markov, I.; Stoyanov, S. Mechanisms of epitaxial growth. *Contemp. Phys.* 1987, 28 (3), 267-320.
- (40) Pertsev, N.; Tagantsev, A.; Setter, N. Phase transitions and strain-induced ferroelectricity in SrTiO₃ epitaxial thin films. *Phys. Rev. B* 2000, 61 (2), R825.
- (41) Damodaran, A. R.; Breckenfeld, E.; Chen, Z.; Lee, S.; Martin, L. W. Enhancement of ferroelectric Curie temperature in BaTiO₃ films via strain-induced defect dipole alignment. *Adv. Mater.* 2014, 26 (36), 6341-6347.
- (42) Cho, Y. J.; Nguyen, N.; Richter, C. A.; Ehrstein, J. R.; Lee, B. H.; Lee, J. C. Spectroscopic ellipsometry characterization of high-k dielectric HfO₂ thin films and the high-temperature annealing effects on their optical properties. *Appl. Phys. Lett.* 2002, 80 (7), 1249-1251.

- (43) Park, J.-W.; Lee, D.-K.; Lim, D.; Lee, H.; Choi, S.-H. Optical properties of thermally annealed hafnium oxide and their correlation with structural change. *J. Appl. Phys.* 2008, 104 (3), 033521.
- (44) Foster, A. S.; Gejo, F. L.; Shluger, A.; Nieminen, R. M. Vacancy and interstitial defects in hafnia. *Phys. Rev. B* 2002, 65 (17), 174117.
- (45) Gritsenko, V. A.; Perevalov, T. V.; Islamov, D. R. Electronic properties of hafnium oxide: A contribution from defects and traps. *Phys. Rep.* 2016, 613, 1-20.
- (46) Xiong, K.; Robertson, J.; Clark, S. Passivation of oxygen vacancy states in HfO_2 by nitrogen. *J. Appl. Phys.* 2006, 99 (4), 044105.
- (47) Xiong, K.; Robertson, J.; Gibson, M.; Clark, S. Defect energy levels in HfO_2 high-dielectric-constant gate oxide. *Appl. Phys. Lett.* 2005, 87 (18), 183505.
- (48) Urbach, F. The long-wavelength edge of photographic sensitivity and of the electronic absorption of solids. *Phys. Rev.* 1953, 92 (5), 1324.
- (49) Mott, N. F.; Davis, E. A. *Electronic processes in non-crystalline materials*; Oxford university press, 2012.
- (50) De Wolf, S.; Holovsky, J.; Moon, S.-J.; Loper, P.; Niesen, B.; Ledinsky, M.; Haug, F.-J.; Yum, J.-H.; Ballif, C. Organometallic halide perovskites: sharp optical absorption edge and its relation to photovoltaic performance. *J. Phys. Chem. Lett.* 2014, 5 (6), 1035-1039.

(51) Choudhury, B.; Choudhury, A. Oxygen defect dependent variation of band gap, Urbach energy and luminescence property of anatase, anatase–rutile mixed phase and of rutile phases of TiO₂ nanoparticles. *Phys. E* 2014, 56, 364-371.

(52) Choudhury, B.; Chetri, P.; Choudhury, A. Annealing temperature and oxygen-vacancy-dependent variation of lattice strain, band gap and luminescence properties of CeO₂ nanoparticles. *J. Exp. Nanosci.* 2015, 10 (2), 103-114.

(53) Sarma, D.; Rao, C. XPES studies of oxides of second-and third-row transition metals including rare earths. *J. Electron Spectrosc. Relat. Phenom.* 1980, 20 (1), 25-45.

(54) Perevalov, T. V.; Prosvirin, I. P.; Suprun, E. A.; Mehmood, F.; Mikolajick, T.; Schroeder, U.; Gritsenko, V. A. The atomic and electronic structure of Hf_{0.5}Zr_{0.5}O₂ and Hf_{0.5}Zr_{0.5}O₂:La films. *J. Sci.: Adv. Mater. Devices* 2021, 6 (4), 595-600.

(55) Ryu, S. W.; Cho, S.; Park, J.; Kwac, J.; Kim, H. J.; Nishi, Y. Effects of ZrO₂ doping on HfO₂ resistive switching memory characteristics. *Appl. Phys. Lett.* 2014, 105 (7), 072102.

(56) Zhou, Y.; Zhang, Y.; Yang, Q.; Jiang, J.; Fan, P.; Liao, M.; Zhou, Y. The effects of oxygen vacancies on ferroelectric phase transition of HfO₂-based thin film from first-principle. *Comput. Mater. Sci.* 2019, 167, 143-150.

Appendix

Section 1. X-ray Reflection, Atomic Force Microscopy, and Full Range X-ray Diffraction for HZO Thin Films on YSZ Substrates

To assess the thickness of the films, X-ray reflection (XRR) measurements were performed on HZO thin films. Figure A1a-c display the XRR scans for each (001), (110), and (111)-oriented epitaxial HZO thin films, respectively. The XRR spectra was fitted using a model with a single HZO layer on a YSZ substrate.¹ By fitting the XRR oscillation data, the growth rates of the thin films were estimated to be 2.0 Å/cycle, 1.8 Å/cycle, and 1.6 Å/cycle for the (001), (110), and (111) crystallographic orientations, respectively. By precisely estimating the thickness of the film, the optical constants of each HZO thin film could be accurately analyzed.

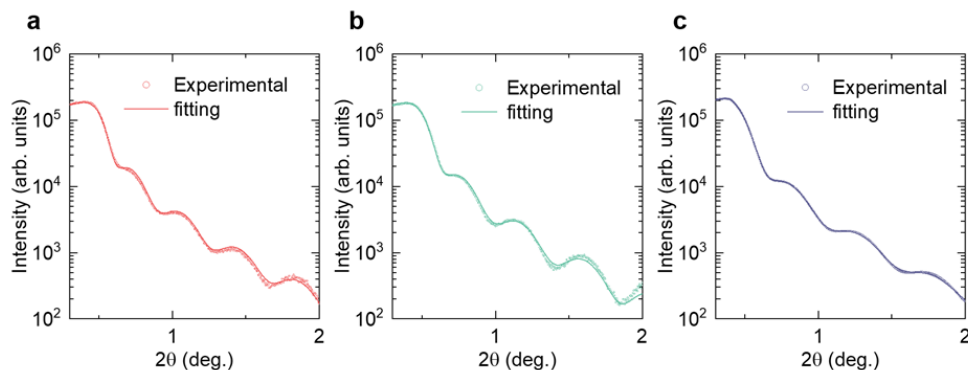


Figure A1. XRR measurement results for epitaxial HZO thin films deposited on (a) (100), (b) (110), and (c) (111) YSZ substrates, respectively. Circles represent the experimental data, while the solid lines represent the fitting results.

The surface morphology and roughness were investigated using atomic force microscopy (AFM). Figure A2a-c show the surface morphology over a $3\ \mu\text{m} \times 3\ \mu\text{m}$ area for (001), (110), and (111)-oriented HZO thin films, respectively. The root mean square (RMS) roughness values for the (001), (110), and (111)-oriented epitaxial HZO thin films are $1.3\ \text{\AA}$, $1.5\ \text{\AA}$, and $1.8\ \text{\AA}$, respectively. The smooth surface assessed by AFM as well as XRR results allowed us to use a two-layer model without considering surface/interface roughness, enabling accurate analysis of the optical constants of the HZO thin films.

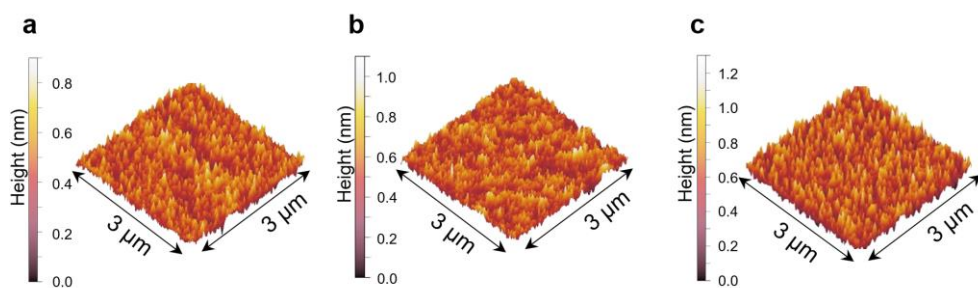


Figure A2. Three-dimensional AFM images illustrating the surface morphology of HZO thin films on (a) (001), (b) (110), and (c) (111) YSZ substrates, respectively.

XRD θ - 2θ scans were conducted over range of 20 - 80° on all samples. As shown in Figure A3a-c, no diffraction peaks were observed other than those corresponding to the orthorhombic/tetragonal $(00l)$, $(l\bar{l}0)$, and (lll) planes for (001), (110), and (111)-oriented HZO film, respectively, indicating the absence of secondary phases. The observed diffraction peaks are attributed to the YSZ substrates and HZO thin films. By verifying epitaxial crystallinity through XRD, we precisely confirmed the crystallinity-controlled epitaxial growth of HZO thin films.

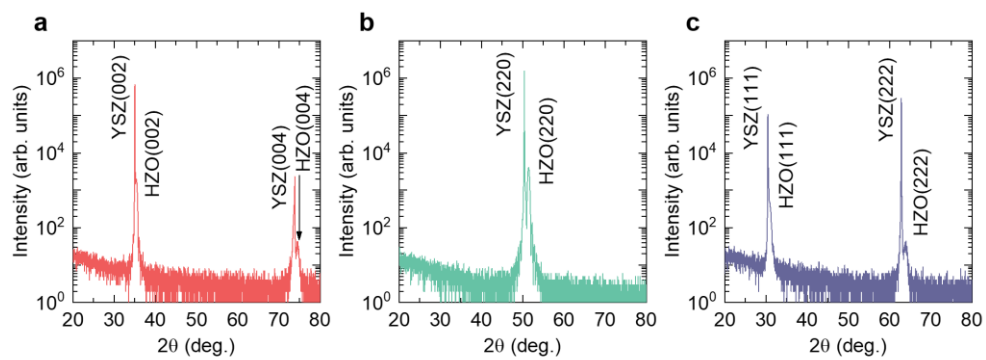


Figure A3. XRD θ - 2θ scan results for epitaxial HZO thin films on (a) (001), (b) (110), and (c) (111) YSZ substrates, respectively.

Section 2. X-ray Reflection, Atomic Force Microscopy, and Full Range X-ray Diffraction for HZO Thin Films on YSZ Substrates

The formation energy of oxygen vacancy in orthorhombic and tetragonal HZO was calculated using the standard density functional theory (DFT) methods implemented in the Vienna Ab initio Simulation Package (VASP) code. We adopted the local density approximation (LDA), to describe the exchange-correlation interactions.²⁻⁴ The cutoff energy for the plane-wave basis was chosen to be 500 eV. The atomic structures of conventional unit cells with 12 atoms were modified to account for biaxial epitaxial strains, and only the out-of-plane cell parameters and atomic positions were optimized using a 6×6×6 Monkhorst-Pack k-point mesh. In contrast, non-strained unit cells were optimized without constraints. The formation energy of oxygen vacancy was calculated based on 72atoms supercell constructed with the optimized unit cells under both strained and non-strained conditions. Oxygen vacancy was calculated as charge-neutral, based on the assumption that the charge is compensated within the total energy calculation of supercells.⁵

Table A1 presents the formation energies of oxygen vacancy calculated using supercells constructed from optimized non-strained unit cells. The calculation of oxygen vacancy formation energy was conducted in the non-strained bulk orthorhombic and tetragonal HZO supercell for the references. Note that the formation energy with strain is listed in the Table 1 of the main manuscript. Each symmetric coordinate was assigned to the position of oxygen atoms in the schematic diagram as shown in Figure 6a, and 6b of the main manuscript. For orthorhombic phase, by comparing the vacancy formation energy between tri-

coordinated and tetra-coordinated oxygen sites, the formation energy of oxygen vacancy was considered only with tetra-coordinated $O_{O(3)}$ and $O_{O(4)}$ sites regardless of strain for the HZO film as mentioned in the main manuscript.

Table A1. DFT-calculated oxygen vacancy formation energy (E_{vac}) for non-strained orthorhombic and tetragonal HZO supercell. The table lists the E_{vac} for different oxygen sites: $O_{O(1)}$, $O_{O(2)}$, $O_{O(3)}$ and $O_{O(4)}$ in orthorhombic phase, and $T_{O(1)}$ and $T_{O(2)}$ in tetragonal phase.

Vacancy sites	Orthorhombic				Tetragonal	
	$O_{O(1)}$	$O_{O(2)}$	$O_{O(3)}$	$O_{O(4)}$	$T_{O(1)}$	$T_{O(2)}$
Formation energy (eV)	7.53	7.65	7.34	7.41	7.37	7.16

Section 3. X-ray Reciprocal Space Mapping Analysis and Strain Calculation for HZO Thin Films on YSZ Substrates

Table A2 presents the lattice constants⁶ and Poisson's ratio⁷ for various HZO polymorphs. To calculate epitaxial strain, and identify potential orthorhombic or tetragonal domains in the thin film, we employed the lattice parameters listed in Table A2 for X-ray RSM analysis. As shown in Figure 1g-i, the lateral coherence between HZO and YSZ in-plane surfaces were fully conserved without the lattice relaxation.

Table A1. Lattice constants and Poisson's ratio of HZO polymorphs.

phase	Lattice length			Lattice angle			Poisson's ratio (v)
	a (Å)	b (Å)	c (Å)	α (°)	β (°)	γ (°)	
Orthorhombic	5.23	5.03	5.05	90	90	90	0.30
Tetragonal	5.04	5.04	5.13	90	90	90	0.30
Monoclinic	5.11	5.18	5.28	90	80	90	0.30

To calculate strain values, we first determined the x and y directions of possible domains by considering lattice constants of HZO polymorphs and crystallographic symmetry operations in the plane groups $\{001\}$, $\{101\}$, and $\{111\}$.⁸ The planes formed by the x and y direction vectors parallel to the YSZ surface are illustrated by the orange planes in Figure 1a-c. The strain values along the x and y directions (η_{xx} , η_{yy}) are calculated by taking into account the lattice

mismatch between the HZO and YSZ unit cells in the x and y directions. The strain values along the z -direction (η_{zz}) are calculated with respect to the calculated η_{xx} , η_{yy} , and a Poisson's ratio of 0.3. The estimated strains and Q_z values derived from η_{zz} are listed in Table A3.

Table A3. Strain calculation for domains in HZO thin films grown on (001), (110), and (111) YSZ substrates. Gray columns indicate domains that do not match the X-ray RSM results or are unobservable in transmission electron microscopy analysis from our prior report.⁹

YSZ surface	Domain	x-direction	y-direction	η_{xx} (%)	η_{yy} (%)	η_{zz} (%)	Q_z
(001)	O-[100]	[010]	[001]	+ 1.789	+ 1.386	- 1.361	0.7754
	O-[010]	[100]	[001]	+ 1.386	- 2.103	+ 0.307	0.7928
	O-[001]	[100]	[010]	- 2.103	+ 1.789	+ 0.135	0.7910
	T-[100]	[010]	[001]	+ 1.587	- 0.195	- 0.597	0.7984
	T-[001]	[100]	[010]	+ 1.587	+ 1.587	- 1.351	0.7905
(110)	O-[110]	[001]	[1 $\bar{1}$ 0]	+ 1.386	- 0.214	- 0.502	0.8317
	O-[101]	[010]	[10 $\bar{1}$]	+ 1.789	- 0.404	- 0.594	0.8307
	O-[011]	[100]	[01 $\bar{1}$]	- 2.103	+ 1.587	+ 0.221	0.8399
	T-[110]	[001]	[1 $\bar{1}$ 0]	- 0.195	+ 1.587	- 0.597	0.8469
	T-[011]	[100]	[01 $\bar{1}$]	+ 1.587	+ 0.684	- 0.974	0.8427
(111)	O-[111]	[1 $\bar{1}$ 0]	[11 $\bar{2}$]	+ 0.844	- 0.214	- 0.270	0.794
	T-[111]	[1 $\bar{1}$ 0]	[11 $\bar{2}$]	- 0.389	+ 1.587	- 0.847	0.804

Section 4. DFT-Calculated Dielectric Functions and Band Structures and of HZO Thin Films on YSZ Substrates

Figure A4a and 4b display DFT-calculated dielectric function of conventional orthorhombic and tetragonal HZO lattices, respectively. Each unit cell was constructed with lattice constant of Table A2. ϵ_a , ϵ_b and ϵ_c correspond to the dielectric function along lattice vectors a, b and c, respectively. With three distinct lattice constant, orthorhombic phase shows biaxial optical anisotropy. And ϵ_b of orthorhombic phase shows pronounced disparity compared to other two components. In tetragonal phase, lattice constant a and b has same value and only c has different lattice length. This structural characteristic is reflected as uniaxial optical anisotropy with same ϵ_a and ϵ_b , whereas ϵ_c shows pronounced difference compared to other two components. Even though, general characteristic of LDA method that underestimate band gaps for semiconductors is shown in figure A4 a, b, we could confirm expected optical anisotropy occurred by structural feature.

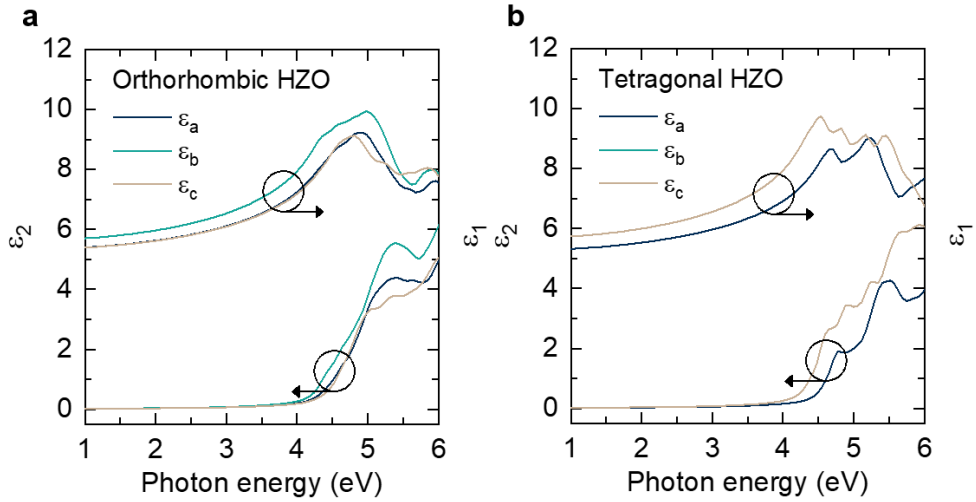


Figure A4. DFT-calculated dielectric functions for conventional (a) orthorhombic and (b) tetragonal HZO lattices. a, b and c correspond to the lattice vectors for each crystal structure respectively.

Figure A5a-g display imaginary part of DFT-calculated dielectric function of HZO domains grown on (001), (110), and (111) YSZ substrate, respectively. To calculate the in-plane (ϵ_x and ϵ_y) and out-of-plane (ϵ_z) components of dielectric function, rectangular cuboid supercells with the cell vectors aligned to the corresponding direction vectors x, y and z of each domain were used, as listed in Table A3. Based on limitation of measuring the optical response in the out-of-plane z-direction caused by the refraction of P-polarized light and the minimal thickness of the film (~ 20 nm), we concentrate on whether in-plane component (ϵ_x and ϵ_y) shows disparity. These calculation results demonstrate (001), (110), and (111)-oriented HZO films might have optical anisotropy

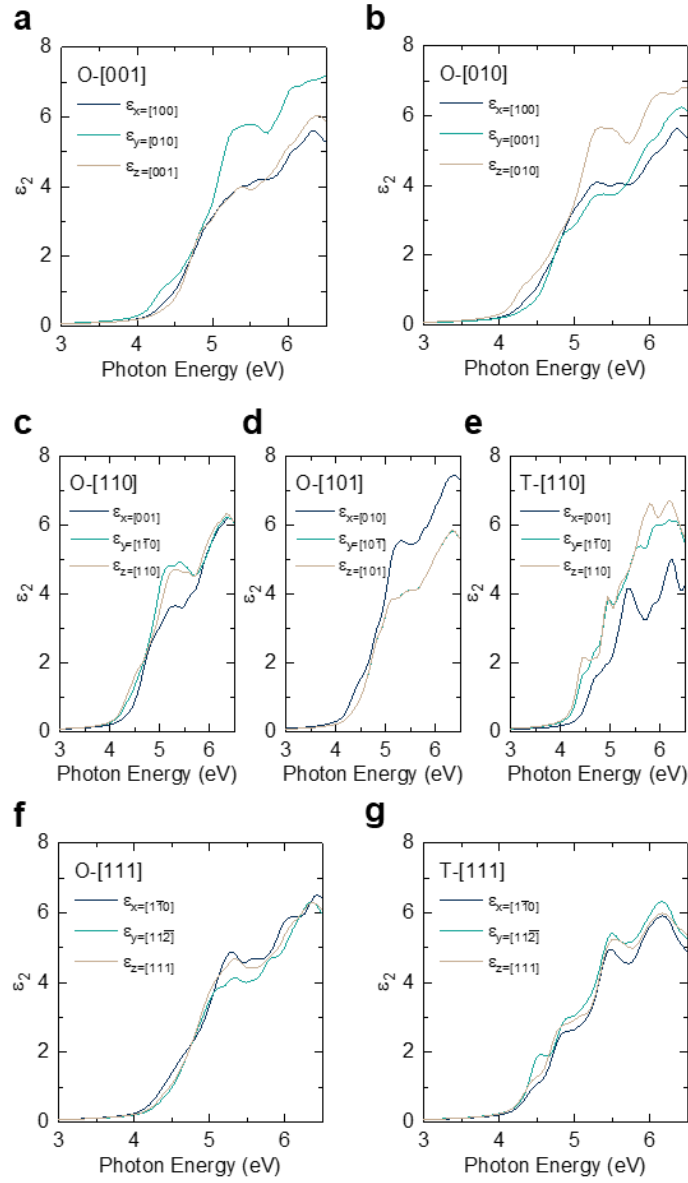


Figure A5. Imaginary part of DFT-calculated dielectric functions for domains in (a,b) (001), (c-e) (110) and (f,g) (111)-oriented epitaxial HZO thin film. x, y and z correspond to the direction vectors of each domain respectively, as listed in Table A3.

Figure A6a and 6b display DFT-calculated band structure and total density of states (TDOS) of non-strained orthorhombic and tetragonal HZO, respectively. x-axis shows high-symmetry directions in each Brillouin zone of orthorhombic phase and tetragonal phase. Orthorhombic phase shows lower bottom of conduction band and TDOS. Estimated direct band gap of orthorhombic phase is 4.14 eV at Y wave vector, while of tetragonal phase is 4.27 eV at Γ wave vector. The lower band gap and TDOS of orthorhombic phase than tetragonal phase implies that our observed direct band gap might be attributed orthorhombic phase.

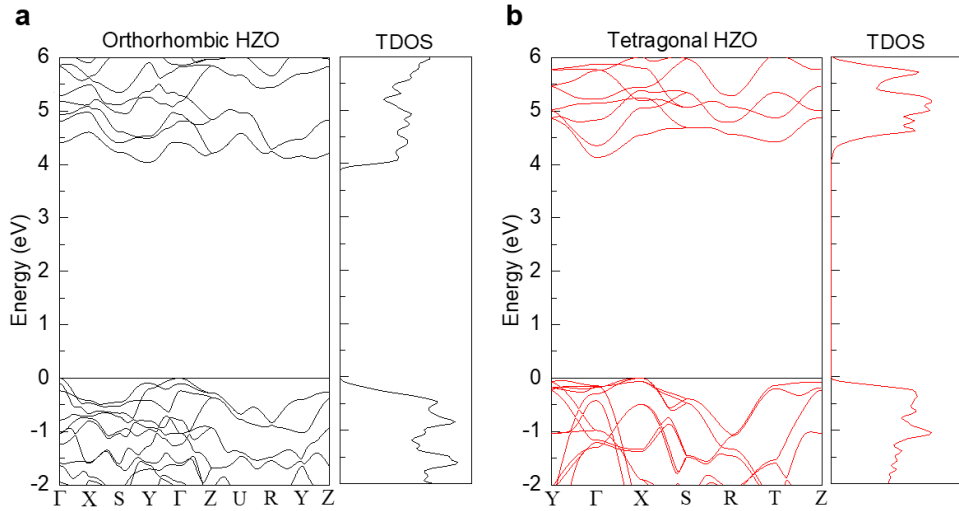


Figure A6. DFT-Calculated electronic band structures and total TDOS of non-strained (a) orthorhombic HZO and (b) tetragonal HZO along high-symmetry directions in the Brillouin zone.

Section 5. Experimental Method for Ellipsometer

Ellipsometry detects changes in polarization of light upon reflection or transmission through a material. These changes are quantified by the amplitude ratio, Ψ , and the phase difference, Δ . The observed response is influenced by the optical properties and thickness of the materials. Consequently, ellipsometry is mainly utilized to ascertain film thickness and optical constants. Additionally, it is employed to analyze composition, crystallinity, surface roughness, doping levels, and other material properties linked to variations in optical response. In this section, we explain the method for measuring ellipsometry parameters using J.A. Woollam's M-2000 and V-VASE equipment, and the process of analyzing these parameters to obtain the optical constants of materials. The figures and operation instructions have been referenced and utilized from the manual provided by J.A. Woollam.

1. Equipment setup

- 1.1. Press the gray power button of control module first, and green power button located at the bottom of the power supply.
- 1.2. Press the lamp power button above the power button of power supply, then press the ignition button to turn on the lamp. After this, check that white light is coming out from the beam source and wait for 15-30 minutes to allow the beam to stabilize.
- 1.3. Next, for the M-2000, run the CompleteEase software, and for the V-VASE, run the WVASE software to initialize the equipment. The M-

2000 will automatically initialize upon starting the program, while for the V-VASE, click the initialize button in the window - hardware tab.

2. Sample loading and alignment

2.1. M-2000

2.1.1. After operating the vacuum switch at the bottom of the ellipsometer, attach the sample to the sample holder.

2.1.2. Set the angle of incidence to 0 degrees and ensure the beam is aligned with the sample. Then, place an opaque paper near the source and adjust the x and y-axis adjustment screws behind the sample holder so that the reflected light from the sample and the light from the source are aligned in a straight line.

2.1.3. Adjust the angle of incidence to the desired measurement angle, then click the “Align Sample” button. Adjust the x and y-axis adjustment screws to center the crossbar, and then use the z-axis adjustment screw to maximize the beam intensity.

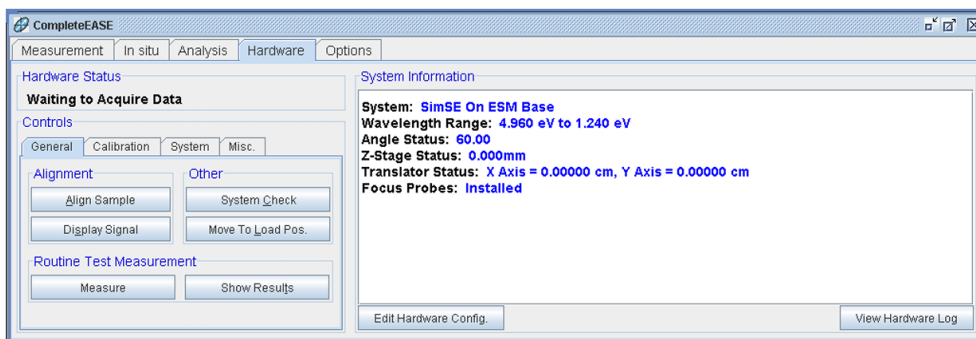


Figure A7. Hardware Tab, showing screen panels and buttons

2.2. V-VASE

- 2.2.1. After operating the vacuum switch at the bottom of the ellipsometer, Load the 25nm Si oxide wafer provided by J.A. Woollam for calibration as the first step.
- 2.2.2. In the Acquire Data menu, perform the following steps in order: Align Sample, Sample Z-Translation Alignment, and Calibrate System.
- 2.2.3. After completing the calibration, load the sample you wish to measure and perform Align Sample and Sample Z-Translation Alignment again.

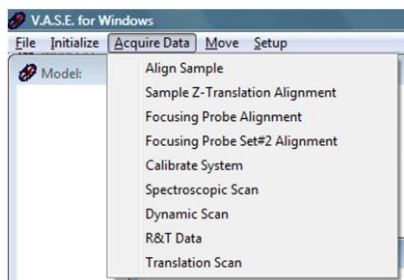


Figure A8. The Acquire Data menu from Hardware window

3. Measurement

3.1. M-2000

3.1.1. Create a recipe for the measurement in the Measurement window.

3.1.2. Set the acquisition parameters such as measurement data type, measurement time.

3.1.3. After setting the saved recipe, press the Measure button to start the measurement.

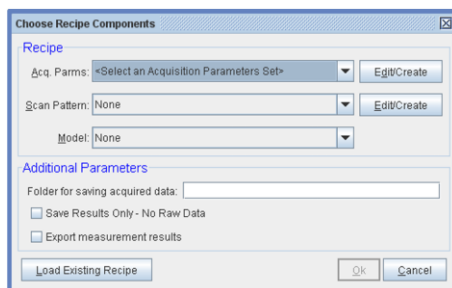


Figure A9. Various components for a recipe

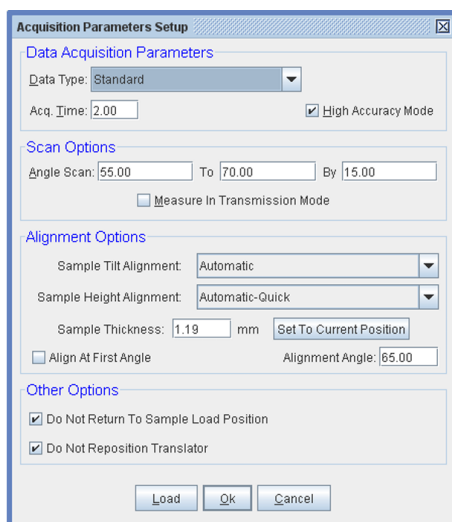
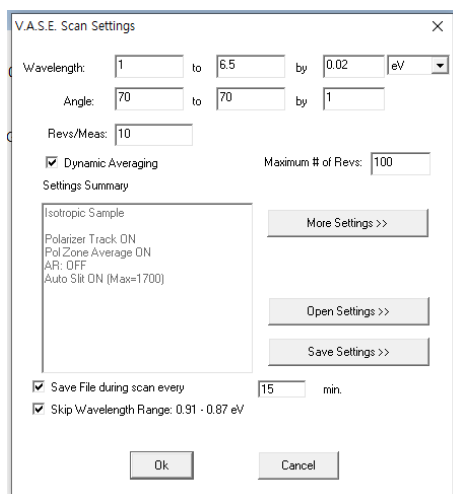


Figure A10. Acquisition parameters setup for M-2000 and RC2 systems

3.2. V-VASE

- 3.2.1. In the Hardware window, under the Acquire Data tab, click on the Spectroscopic Scan tab.
- 3.2.2. Set the measurement wavelength range, angle, and analyzer revolutions, then click the More Settings button.
- 3.2.3. Without changing any other settings unless necessary, select the sample type according to your sample and set the auto retarder to high accuracy mode.



V.A.S.E. Scan Settings

Wavelength: 1 to 6.5 by 0.02 eV

Angle: 70 to 70 by 1

Revs/Meas: 10

☒ Dynamic Averaging Maximum # of Revs: 100

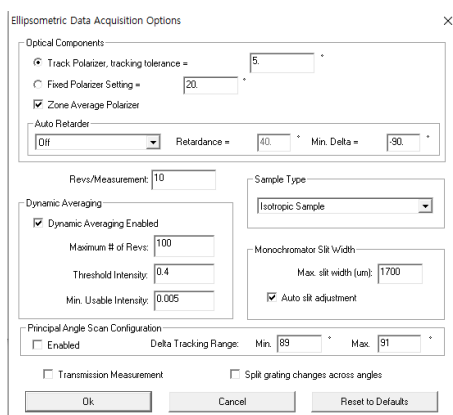
Settings Summary

Isotropic Sample
Polarizer Track ON
Pol Zone Average ON
AR: OFF
Auto Slit ON (Max=1700)

☒ Save File during scan every 15 min.

☒ Skip Wavelength Range: 0.91 - 0.87 eV

Figure A11. Dialog box used to control spectroscopic, variable-angle ellipsometric data scans.



Ellipsometric Data Acquisition Options

Optical Components

☒ Track Polarizer, tracking tolerance = 5

☐ Fixed Polarizer Setting = 20

☒ Zone Average Polarizer

Auto Retarder: Off Retardance = 40 Min. Delta = -90

Revs/Measurement: 10

Dynamic Averaging

☒ Dynamic Averaging Enabled

Maximum # of Revs: 100

Threshold Intensity: 0.4

Min. Usable Intensity: 0.005

Sample Type

Isotropic Sample

Monochromator Slit Width

Max. slit width (um): 1700

☒ Auto slit adjustment

Principal Angle Scan Configuration

☐ Enabled Delta Tracking Range: Min. 89 Max. 91

☐ Transmission Measurement ☐ Split grating changes across angles

Figure A12. Ellipsometric data acquisition options dialog box.

References

- (1) Björck, M.; Andersson, G. GenX: an extensible X-ray reflectivity refinement program utilizing differential evolution. *J. Appl. Crystallogr.* 2007, 40 (6), 1174-1178.
- (2) Kohn, W.; Sham, L. J. Self-consistent equations including exchange and correlation effects. *Phys. Rev.* 1965, 140 (4A), A1133.
- (3) Perdew, J. P.; Wang, Y. Accurate and simple analytic representation of the electron-gas correlation energy. *Phys. Rev. B* 1992, 45 (23), 13244.
- (4) Perdew, J. P.; Zunger, A. Self-interaction correction to density-functional approximations for many-electron systems. *Phys. Rev. B* 1981, 23 (10), 5048.
- (5) Hoffmann, M.; Schroeder, U.; Schenk, T.; Shimizu, T.; Funakubo, H.; Sakata, O.; Pohl, D.; Drescher, M.; Adelman, C.; Materlik, R. Stabilizing the ferroelectric phase in doped hafnium oxide. *J. Appl. Phys.* 2015, 118 (7), 072006.
- (6) Materlik, R.; Künneth, C.; Kersch, A. The origin of ferroelectricity in $\text{Hf}_{1-x}\text{Zr}_x\text{O}_2$: A computational investigation and a surface energy model. *J. Appl. Phys.* 2015, 117 (13), 134109.
- (7) De Jong, M.; Chen, W.; Angsten, T.; Jain, A.; Notestine, R.; Gamst, A.; Sluiter, M.; Krishna Ande, C.; Van Der Zwaag, S.; Plata, J. J. Charting the

complete elastic properties of inorganic crystalline compounds. *Sci. Data* 2015, 2 (1), 1-13.

(8) Liu, S.; Hanrahan, B. M. Effects of growth orientations and epitaxial strains on phase stability of HfO₂ thin films. *Phys. Rev. Mater.* 2019, 3 (5), 054404.

(9) Cho, J. W.; Song, M. S.; Choi, I. H.; Go, K. J.; Han, J.; Lee, T. Y.; An, C.; Choi, H. J.; Sohn, C.; Park, M. H. Atomic Layer Deposition of Epitaxial Ferroelectric Hf_{0.5}Zr_{0.5}O₂ Thin Films. *Adv. Funct. Mater.* 2024, 34 (24), 2314396.

국문 초록

이 논문에서는 원자층 증착법을 이용해 (001), (110), (111) 표면 방향으로 성장한 단결정형 $\text{Hf}_{0.5}\text{Zr}_{0.5}\text{O}_2$ 박막의 광학적 반응을 분석하여 산소 변형이 박막 내 산소 결핍 형성에 미치는 선택적 영향을 보고한다. $\text{Hf}_{0.5}\text{Zr}_{0.5}\text{O}_2$ 박막들은 yttria-stabilized zirconia 기판 위에 성장되었으며, 해당 박막들에 대해 자외선-가시광선 타원 편광 분석기를 통해 광학적 분광 분석을 수행하였다. (111) 표면 방향의 $\text{Hf}_{0.5}\text{Zr}_{0.5}\text{O}_2$ 박막에서 shallow trap level 이 단독적으로 관찰되었으며 또한 X-선 광전자 분광법을 통한 분석 결과 다른 표면 방향의 박막들과 비교하여 강한 산소 결핍 생성 신호를 가짐을 확인하였다. 산소 공공 형성 에너지에 대한 밀도 범함수 이론 기반 계산 또한 (111) 표면 방향으로 성장한 박막의 산소 결핍에 대한 뚜렷한 신호를 보여주었다. 이러한 (111) 표면 방향의 $\text{Hf}_{0.5}\text{Zr}_{0.5}\text{O}_2$ 박막에서 선택적인 산소 공공 형성은 기능성 $\text{Hf}_{0.5}\text{Zr}_{0.5}\text{O}_2$ 박막에서 산소 결함과 관련된 잠재적 현상이 부분적으로 (111) 방향의 변형에 기인함을 시사한다.

주요어 : 산소 공공, 결함, 산화물 하프늄 지르코늄, 단결정형, 박막

학번 : 2022-27471